materials

Article

Efficient Solar-Induced Photoelectrochemical Response Using Coupling Semiconductor TiO$_2$-ZnO Nanorod Film

Nur Azimah Abd Samad, Chin Wei Lai *, Kung Shiuh Lau and Sharifah Bee Abd Hamid

Nanotechnology & Catalysis Research Centre (NANOCAT), 3rd Floor, Block A,
Institute of Postgraduate Studies (IPS), University of Malaya, 50603 Kuala Lumpur, Malaysia;
nurazimah@um.edu.my (N.A.A.S.); lauks@um.edu.my (K.S.L.); sharifahbee@um.edu.my (S.B.A.H.)
* Correspondence: cwlai@um.edu.my; Tel.: +60-3-7967-6960

Abstract: Efficient solar driven photoelectrochemical (PEC) response by enhancing charge separation has attracted great interest in the hydrogen generation application. The formation of one-dimensional ZnO nanorod structure without bundling is essential for high efficiency in PEC response. In this present research work, ZnO nanorod with an average 500 nm in length and average diameter of about 75 nm was successfully formed via electrodeposition method in 0.05 mM ZnCl$_2$ and 0.1 M KCl electrolyte at 1 V for 60 min under 70 °C condition. Continuous efforts have been exerted to further improve the solar driven PEC response by incorporating an optimum content of TiO$_2$ into ZnO nanorod using dip-coating technique. It was found that 0.25 at % of TiO$_2$ loaded on ZnO nanorod film demonstrated a maximum photocurrent density of 19.78 mA/cm^2 (with V vs. Ag/AgCl) under UV illumination and 14.75 mA/cm^2 (with V vs. Ag/AgCl) under solar illumination with photoconversion efficiency ~2.9% (UV illumination) and ~4.3% (solar illumination). This performance was approximately 3–4 times higher than ZnO film itself. An enhancement of photocurrent density and photoconversion efficiency occurred due to the sufficient Ti element within TiO$_2$-ZnO nanorod film, which acted as an effective mediator to trap the photo-induced electrons and minimize the recombination of charge carriers. Besides, phenomenon of charge-separation effect at type-II band alignment of Zn and Ti could further enhance the charge carrier transportation during illumination.

Keywords: TiO$_2$-ZnO composite thin film; ZnO nanorod; TiO$_2$ nanoparticles; photocurrent response

1. Introduction

ZnO nanostructure is a rapidly developing metal oxide. The dynamic design and promising functional properties attract momentous scientific interest. With its vast nano-architecture, ZnO nanorod shape is the most studied photocatalyst in photoelectrochemical (PEC) response. As mentioned above, noticeable limitation, specifically its poor solar illumination absorption and rapid recombination charge carrier losses, hinder further practice in electronic application. In general, copious researches proved that performance of ZnO nanorod photocatalyst (solar illumination absorption and recombination of charge carrier losses) could be improved by coupling with another semiconductor photocatalyst [1,2]. Therefore, the objective of this research work is to study the PEC system performance from TiO$_2$-ZnO nanocomposite photoelectrode under ultraviolet (UV) and solar illumination. The novelty lies via the simple combination of electrodeposition and dip-coating that have not been approached by any other researcher (Table 1).

ZnO nanorods can be formed from sol-gel method [3,4], hydrothermal method [5–10], solvothermal method [11–14], chemical vapor deposition (CVD) method [15–18], atomic layer deposition (ALD) method [19–22], electrodeposition method [23–26], and other methods. However,

due to several advantages, electrodeposition method has been chosen for the formation of ZnO nanorods in this research work. The advantages of electrodeposition method are that it is simple, quick, and economic; able to control the crystallization of ZnO nanorods [27]; its low temperature condition and low equipment cost; and the precise controllability and repeatability of nanostructures [28]. There are a few unique elements in electrodeposition process used in this research work. First, the rarely-used zinc substrate, which helps improve the electron movement from TiO_2-ZnO to external circuit. Second, it is template-free and seed layer-free. Third, no additional acid was applied in controlling electrolyte pH during electrodeposition process. This combination brought the difference of electrodeposition method in this research work from previous work. Further explanation is included in Section 3.1.

Furthermore, the modification of binary oxide that arises from the enrichment of second oxide on primary oxide diminishes radiationless transfer of the photon energy absorbed by second oxide [29]. In addition, Anpo et al. have proven that the enhancement of the photocatalytic activity of the TiO_2 species in the primary oxide have a lower Ti content [29]. The coupling of two semiconductors with appropriate energy, CB and VB, can reduce the recombination of e^-/h^+ pairs due to the transfer of carriers from one semiconductor to the other. Furthermore, depending on the band-gap energy of the semiconductor used, the composite can be activated in the visible region [30]. The interfacial potential gradient, corresponding to the energetic position, plays a role by providing better charge carrier transportation, and charge carrier separation can be achieved by modification of core photocatalyst [31,32].

When the core photocatalyst coupled with another semiconductor is activated by illumination, electrons are injected from the semiconductor with a more negative conduction band (CB) level to the positive one, while holes are transferred from the semiconductor with a more positive valence band (VB) level to the negative one. Thus, separation of charge carriers could be achieved; consequently, the lifetime of the charge carriers and the efficiency of the interfacial charge transfer to water increase significantly [7]. Details of hybrid TiO_2-ZnO formation based on different method from past researchers are summarized in Table 1. Optimum amount of incorporated TiO_2-based ZnO formation results in extended lifetimes of charge carriers and suppression of the recombination losses effectively. The modification of ZnO could lead to higher photocatalytic activity than ZnO itself. Besides, the improvement in light absorption occurred from UV region to visible region.

Table 1. The development of hybrid TiO_2-ZnO formation based on different approaches.

Authors	Method	Findings	Reference
Dali Shao et al. (2014)	• Hydrothermal (ZnO nanowires) • Atomic layer deposition (TiO_2 shell)	• Two steps fabrication ZnO-TiO_2 core shell nanowires. For UV sensing application. • UV illumination efficiently reduced band-to-band recombination. • Maximum photoresponsivity with 495 A/W at 373 nm under −10 V.	[33]
Simelys Hernández et al. (2014)	• Seed layer-assisted hydrothermal route (ZnO nanowires) • In situ non-acid sol–gel synthesis (TiO_2 shell)	• Photocurrent densities, values of about 0.7 mA/cm^2 under simulated solar light (AM1.5 G, 100 mW/cm^2). • The core–shell photo-anodes performance was about twice and forty-times better than the ones with a film of equivalent thickness of bare ZnO NWs and TiO NPs, respectively.	[34]
Dao et al. (2013)	• Hydrothermal (ZnO nanowires) • Sol-gel (TiO_2 shell)	• UV photodetector. • Heterojunction is composed of a 5–10 nm thick p-type Cr-doped TiO_2 nanoshell and n-type single-crystalline ZnO nanowires (50 nm radius). • At a moderate reverse bias of −5 V and under UV illumination at 104 μW, it showed a switch current ratio of 140 μW and a responsivity as large as 250 A/W, while it showed nearly no response to the infrared and visible light.	[35]
Lin Lin et al. (2012)	• Hydrothermal method	• TiO_2-ZnO n–p–n heterojunction nanorod with diameter of 30 nm. • Photodegrading methyl orange has been demonstrated to increase three times compared to that of wurtzite hexagonal ZnO.	[36]
Shrabani Panigrahi et al. (2011)	• Aqueous chemical technique (ZnO nanorod) • Solution of titanium isopropoxide [Ti (OC3 H7)$_4$] followed by a heating to form the shell (TiO_2 shell).	• UV sensor application. • The UV photosensitivity of the nanocomposite becomes four times larger while the photocurrent decay during steady UV illumination has been decreased almost by 7 times compared to the as-grown ZnO NRs indicating high efficiency of these core–shell structures.	[37]

2. Results and Discussion

2.1. Morphological Studies

　　After electrodeposition and dip-coating methods, TiO_2-ZnO can be found on both sides of the electrode. Each additional dip-coating cycle produced a small change in TiO_2-ZnO thin film morphology (Figure 1). Meanwhile, Figure 2 shows the schematic diagram of dip-coating method for the formation of TiO_2 loaded-ZnO. Average compositional ratio for ZnO, one-cycle dip-coating TiO_2-ZnO, two-cycle dip-coating TiO_2-ZnO, and three-cycle dip-coating TiO_2-ZnO are shown in Table 2 using EDX spectroscopy analysis. From here, samples are named after the titanium atomic percentage (at %). One-cycle dip-coating TiO_2-ZnO, two-cycle dip-coating TiO_2-ZnO, and three-cycle dip-coating TiO_2-ZnO are named 0.25 at %, 0.50 at %, and 1.0 at %, respectively. FESEM images show that all samples were very nearly vertically aligned and were of the average length, diameter and aspect ratio shown in Table 3. In addition, Figure 1a–d shows a decrease in the length and diameter with the increase in dip-coating cycles. This result is attributed to the etching phenomenon by the TiO_2 solution which was in an acidic (pH 1–3) solution to maintain the dispersion of TiO_2. From the HRTEM result, there was a boundary that split the two different materials (Figure 1e). This was confirmed by the lattice spacing by each material: 0.27 nm (ZnO (002)) and 0.33 nm (TiO_2). In addition, the existence of the two different materials could be recognized by the arrangement of atoms in different directions.
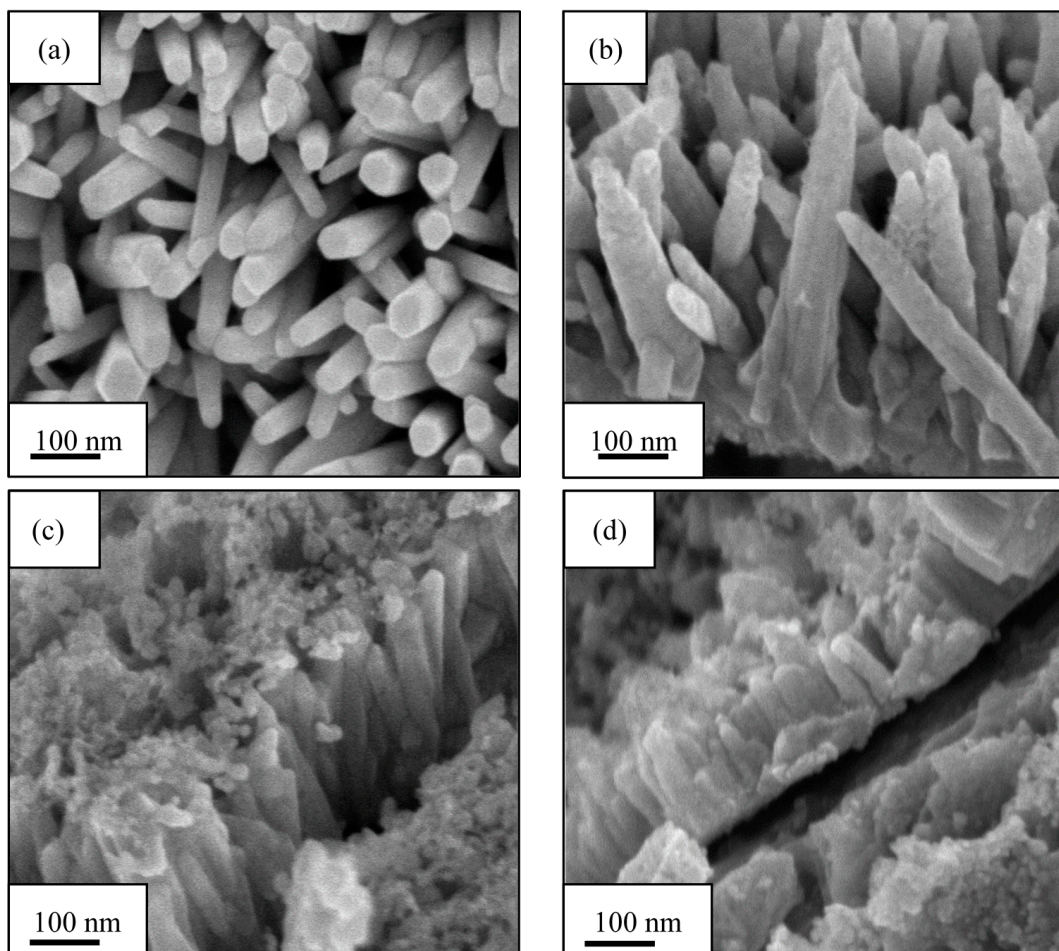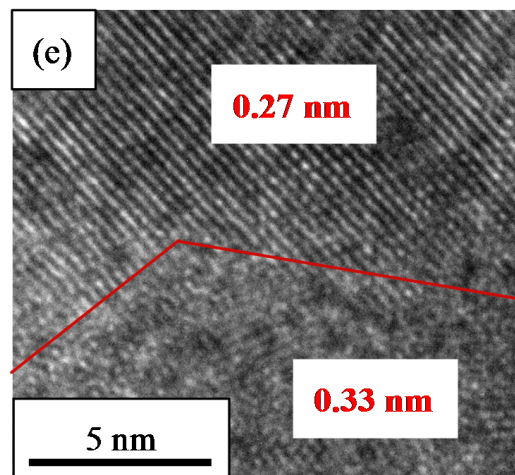

Figure 1. *Cont.*

Figure 1. FESEM images with 100 k magnification: (**a**) ZnO; (**b**) 0.25 at % TiO$_2$-ZnO; (**c**) 0.50 at % TiO$_2$-ZnO; and (**d**) 1.0 at % TiO$_2$-ZnO; (**e**) HRTEM image for TiO$_2$-ZnO.
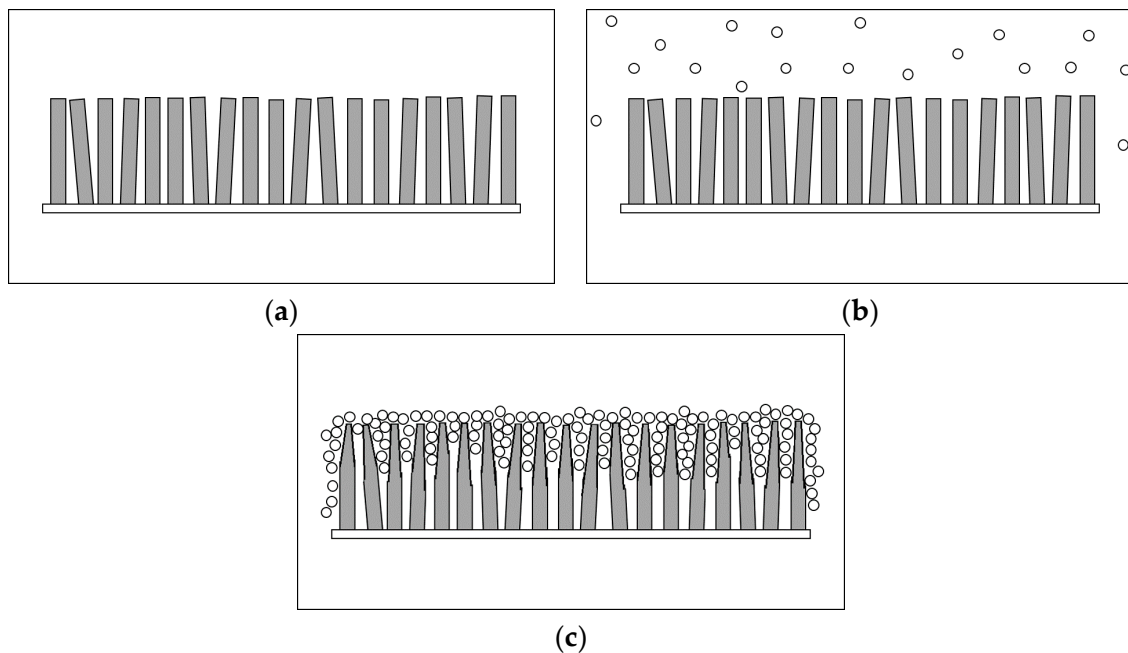

Figure 2. The schematic diagram of dip-coating method for the formation of TiO$_2$ loaded-ZnO: (**a**) ZnO nanorods; (**b**) dip-coating process; and (**c**) TiO$_2$ loaded-ZnO and followed by calcination process at 400 °C.

Table 2. Average compositional ratio for ZnO, one-cycle dip-coating TiO$_2$-ZnO, two-cycle dip-coating TiO$_2$-ZnO, and three-cycle dip-coating TiO$_2$-ZnO using EDX spectroscopy analysis.

Sample	Atomic Percentage (at %)		
	Zinc	**Oxygen**	**Titanium**
ZnO	44.54	55.46	*Nil.*
One-cycle dip-coating TiO$_2$-ZnO	52.95	46.80	0.25
Two-cycle dip-coating TiO$_2$-ZnO	53.25	46.29	0.46
Three-cycle dip-coating TiO$_2$-ZnO	61.96	36.98	1.06

Table 3. The average value of length, diameter and aspect ratio for ZnO, 0.25 at % TiO$_2$-ZnO, 0.50 at % TiO$_2$-ZnO, and 1.0 at % TiO$_2$-ZnO.

Sample	Length (nm)	Diameter (nm)	Aspect Ratio
ZnO	~500	~75	6.7
0.25 at % TiO$_2$-ZnO	~500	~65	7.7
0.50 at % TiO$_2$-ZnO	~350	~60	5.8
1.0 at % TiO$_2$-ZnO	~350	~55	6.4

2.2. Crystallinity Studies

Figure 3 shows the XRD pattern for 0.25 at % TiO$_2$-ZnO, 0.5 at % TiO$_2$-ZnO, 1.0 at % TiO$_2$-ZnO and ZnO thin film. In Figure 3b–d, peaks of TiO$_2$ and ZnO could be observed. TiO$_2$ is denoted by 25.4° (101), 37.3° (103), 38.2° (004), 38.9° (112), 48.3° (200), 54.0° (105), 55.5° (211), and 63.2° (204) (ICDD 01-073-1764). Meanwhile, ZnO is denoted by 31.9° (100), 34.6° (002), 36.2° (101), 47.4° (102), 56.4° (110), 62.9° (103), 68.1° (112), and 69.0° (201) (ICDD 01-080-0074). Increasing the dip-coating cycle produced a lower intensity of FWHM of ZnO. This is because the TiO$_2$ volume started to increase. Moreover, TiO$_2$ loaded on ZnO nanorod film showed that no other elements exist. The quantification 0.25 at % TiO$_2$-ZnO, 0.5 at % TiO$_2$-ZnO, and 1.0 at % TiO$_2$-ZnO were noted as 25%–75%, 34%–66%, and 33%–67%, respectively. Meanwhile, ZnO can be indexed to wurtzite ZnO (ICDD 00-036-1451) without any impurity peaks (Figure 3a). Good crystallinity can be seen from the sharp peaks of ZnO prior to the dip-coating method for TiO$_2$-ZnO.
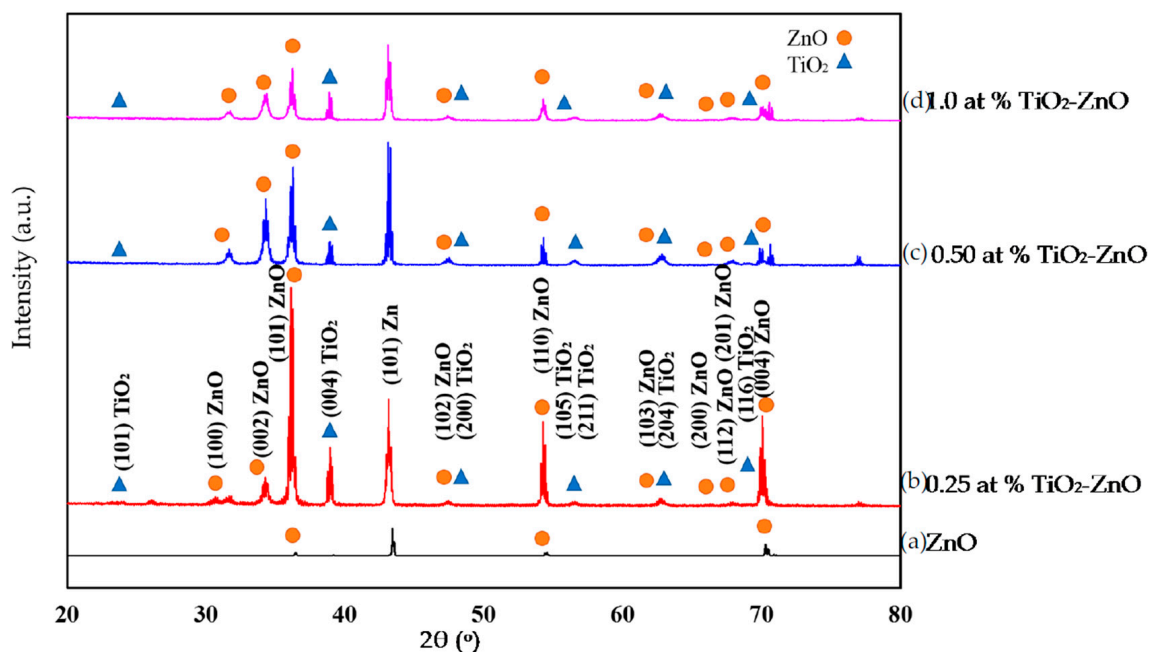
Figure 3. XRD pattern of (**a**) ZnO; (**b**) 0.25 at % TiO$_2$-ZnO; (**c**) 0.50 at % TiO$_2$-ZnO; and (**d**) 1.0 at % TiO$_2$-ZnO.

Raman analysis was used to determine and understand the structural changes of ZnO and TiO$_2$ upon increasing the dip-coating cycle. However, Figure 4 shows no signature of the TiO$_2$ substance, with the Raman peaks mainly belonging to wurtzite ZnO. This might be due to the very small amount of TiO$_2$ and to the scattering spectra that could be negligible as they were too small to be seen. These thin films were still weak in stoichiometric ZnO due to the dominance of the E$_1$ (LO) and A$_1$ (LO) modes (570–585 cm^{-1}) for all samples compared to the E$_2$ (high) mode 438 cm^{-1}. This can be explained by the oxygen atom deficiency that was represented by these two modes (E$_1$ (LO) and A$_1$ (LO) mode (570–585 cm^{-1})) and with the existence of the Zn element from the Zn substrate [38,39]. Increasing the

dip-coating cycle produced a lower E_2 (high) mode, which was attributed to the depreciation of the perfect crystal structure wurtzite ZnO. Meanwhile, as mentioned above, there was a dominance of the E_1 (LO) and A_1 (LO) mode (570–585 cm^{-1}) for all samples compared to the E_2 (high) mode 438 cm^{-1}. However, an increase in the dip-coating cycle produced a slight depreciation in the E_1 (LO) and A_1 (LO) modes. Increasing the dip-coating cycle decreased the absorption of light, producing slightly lower Raman spectra. This argument is supported by reflectance spectra under section 2.5 Optical Properties (Figure 15). The small shift of spectra was probably due to the optical phonon confinement, a defect or impurity in the nanocrystal, laser irradiation heating, or the tensile strain effect [40,41].
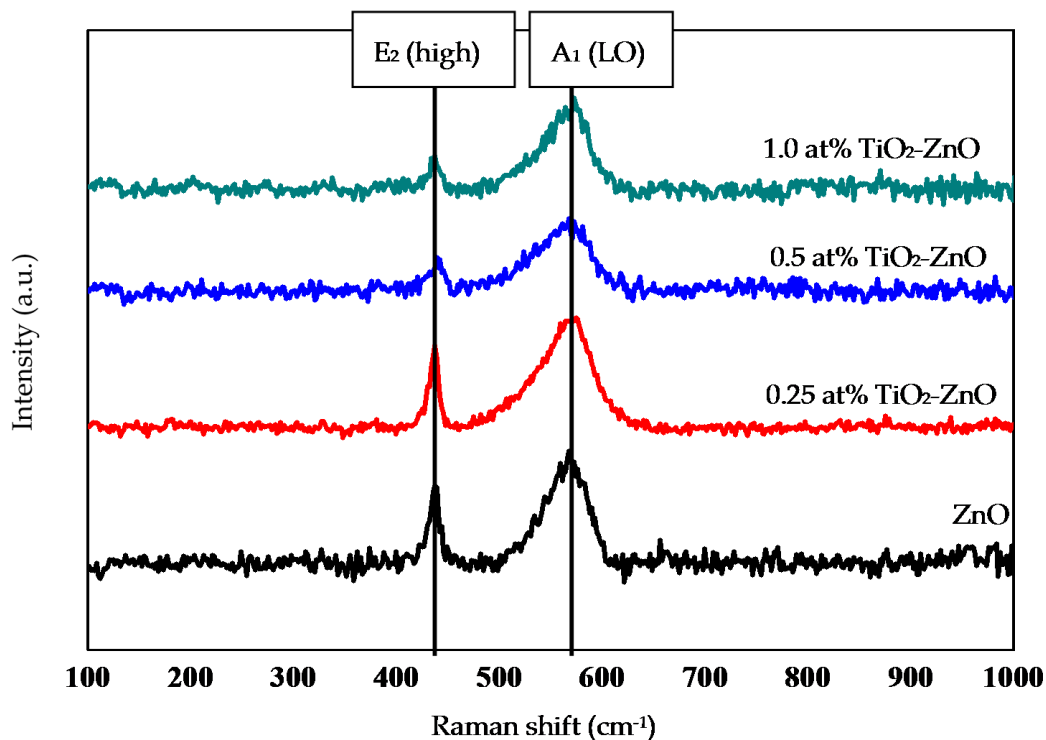

Figure 4. Raman scattering of ZnO, 0.25 at % TiO$_2$-ZnO, 0.5 at % TiO$_2$-ZnO, and 1.0 at % TiO$_2$-ZnO.

For a further understanding of the elements and chemical interaction of the TiO$_2$-ZnO interface, a XPS analysis was carried out for samples ZnO, 0.25 at % TiO$_2$-ZnO and 1.0 at % TiO$_2$-ZnO. XPS survey spectra confirmed that TiO$_2$ was successfully deposited onto the ZnO film. The elements Zn, Ti, C, and O existed in the TiO$_2$-ZnO nanorods (Figure 5). The XPS results showed that the Ti peaks increased with the dip-coating cycle. This is in accordance with the EDX results. One peak of Zn2p$_{3/2}$ was detected at binding energy 1021 $\pm$ 1.0 eV (Figure 6) and this matched the CAS registry No. 1314-13-2, referring to National Institute of Standards and Technology (NIST), an agency of the U.S. Department of Commerce [42]. From this, the sample with the formula ZnO is classed as a catalyst and an oxide with the line designation 2p$_{3/2}$ and a related-binding energy of 1021 $\pm$ 1.0 eV [43]. With the increase in the dip-coating cycle, the binding energy of Zn2p$_{3/2}$ shifted to a lower binding energy (Figure 6). The difference in binding energies is attributed to the change of charge transfer from Zn^{2+} to O^{2-}. In addition, previous research has shown that oxygen deficiency is the main factor in the decrease in binding energy [44,45]. This argument was supported by the Zn2p and O1s binding energies were shifted to lower binding energies after the coating method. The XPS results showed a decrease in the Zn/O ratio for TiO$_2$ loaded on ZnO nanorod film as compared to the ZnO itself.
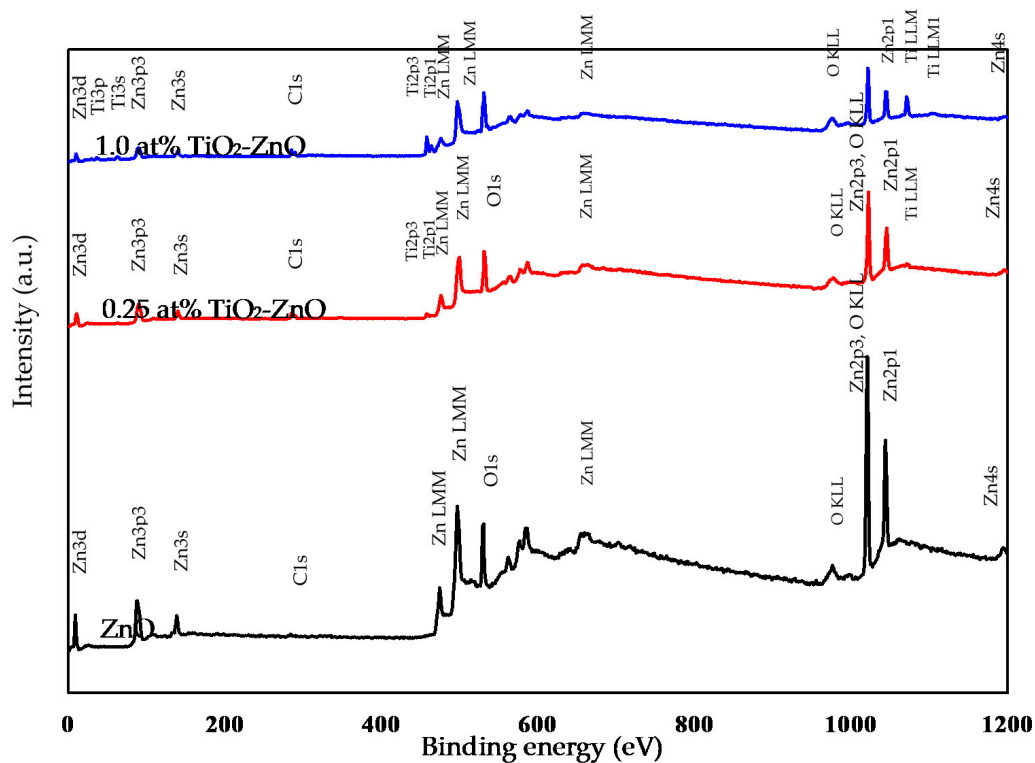
Figure 5. Full XPS survey spectra of ZnO, 0.25 at % TiO$_2$-ZnO, and 1.0 at % TiO$_2$-ZnO.
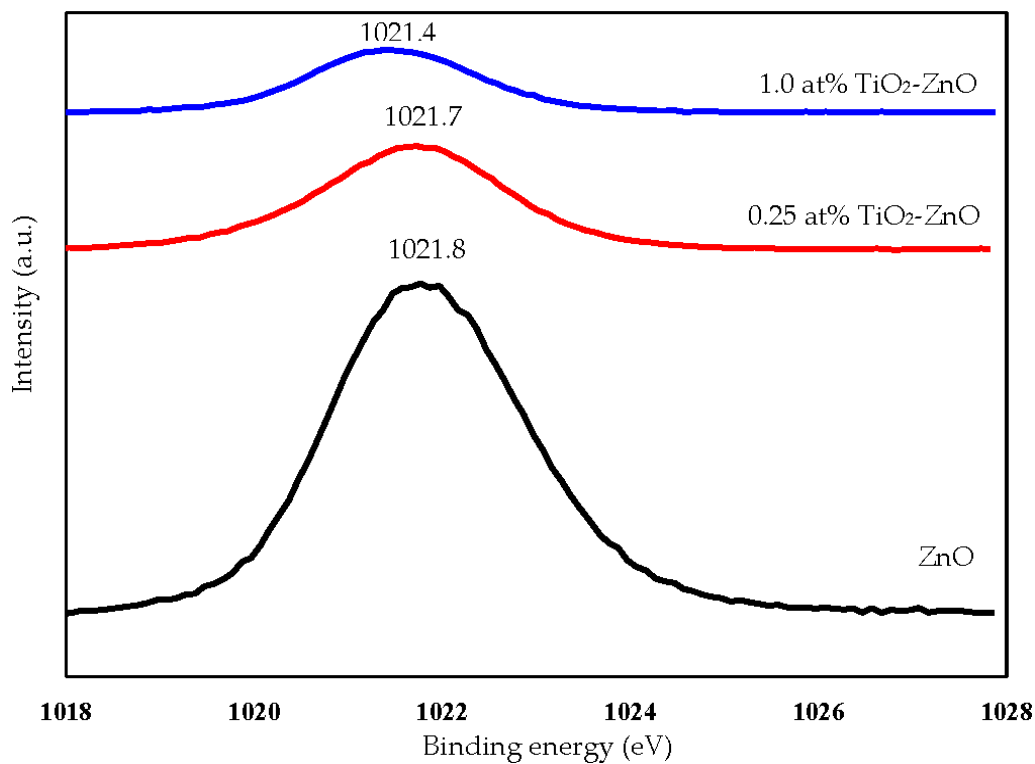

Figure 6. XPS spectra Zn2p of ZnO, 0.25 at % TiO$_2$-ZnO, and 1.0 at % TiO$_2$-ZnO.

Referring to Zhang et al. and Al-Gaashani et al., O1s binding energies at 530.4 eV, 531.4 eV, and 532.4 eV are O^{2-} species in the lattice (O_L), oxygen vacancies and defects (O_v), and chemisorbed or dissociated (O_c) oxygen species, respectively [46,47]. Meanwhile, the O1s binding energies associated in all samples in this research work are 530.5 eV (ZnO), 529.7 eV and 531.7 eV (1.0 at % TiO_2-ZnO), 531.7 eV (0.25 at % TiO_2-ZnO), and 530.0 eV (TiO_2). It can be clearly seen that all O1s curves were asymmetric; therefore, both lines were fitted with two Gaussian peaks (I and II) (Figure 7 (1.0 at % TiO_2-ZnO)). Peak I of O1s was located in the lower binding energy, as compared to peak II. Peak I was assigned for the O^{2-} ions of the Zn-O bonding at the crystal lattice (O_L) [46,48]. For peak II (1.0 at % TiO_2-ZnO), the location of 531.7 eV is located in between oxygen vacancies defect (531.4 eV) and existence of hydroxyl group (532.4 eV). From the EDX result, it was confirmed that O at % is reduced with the increase in the dip-coating cycle (Table 2). However, the existence of –OH group is accepted as Zn-OH formed before the formation of ZnO. These hydroxyl groups helped to prevent the recombination of electron–holes [44,49].
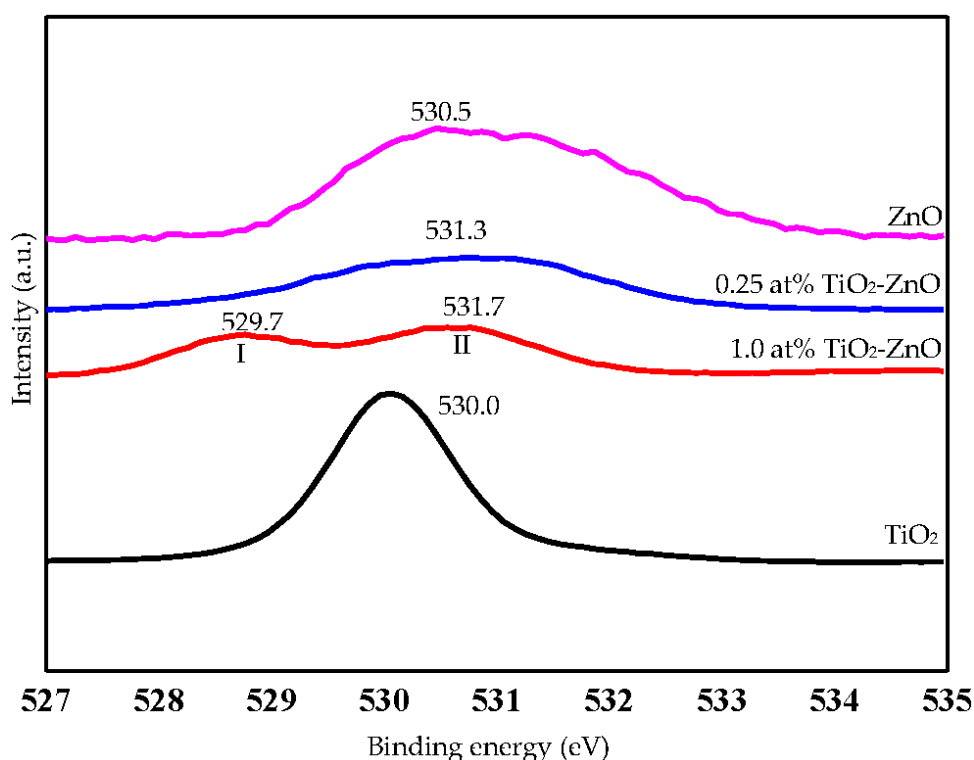

Figure 7. XPS spectra O1s of TiO_2, 0.25 at % TiO_2-ZnO, 1.0 at % TiO_2-ZnO, and ZnO.

The XPS spectra for Ti2p showed binding energies at 458.8 and 464.5 eV, demonstrating $Ti2p_{3/2}$ and $Ti2p_{1/2}$, respectively [50–55]. The Ti2p spectra indicated that the Ti in TiO_2-ZnO were all in a Ti^{4+} state, but the heterogeneous environments of Ti^{4+} resulted in the broadening of the Ti^{4+} 2p in the XPS spectra. There is a slight decrease in the intensity of the $Ti2p_{3/2}$ peak and a broadening of the $Ti2p_{1/2}$ with an increase in the Ti/Zn ratio from 1.0 at % to 0.25 at % (Figure 8). This indicated a decrease in the Ti^{4+} state and the heterogeneous environment due to high intensity of ZnO as compared to TiO_2. In addition, we can see that binding energies of TiO_2 are shifting to lower binding energies because it has been coupled with the electron rich material ZnO (Figure 8). The existence of C1s belongs to containment carbon during calibration. A summary of XPS spectra is presented in Table 4.
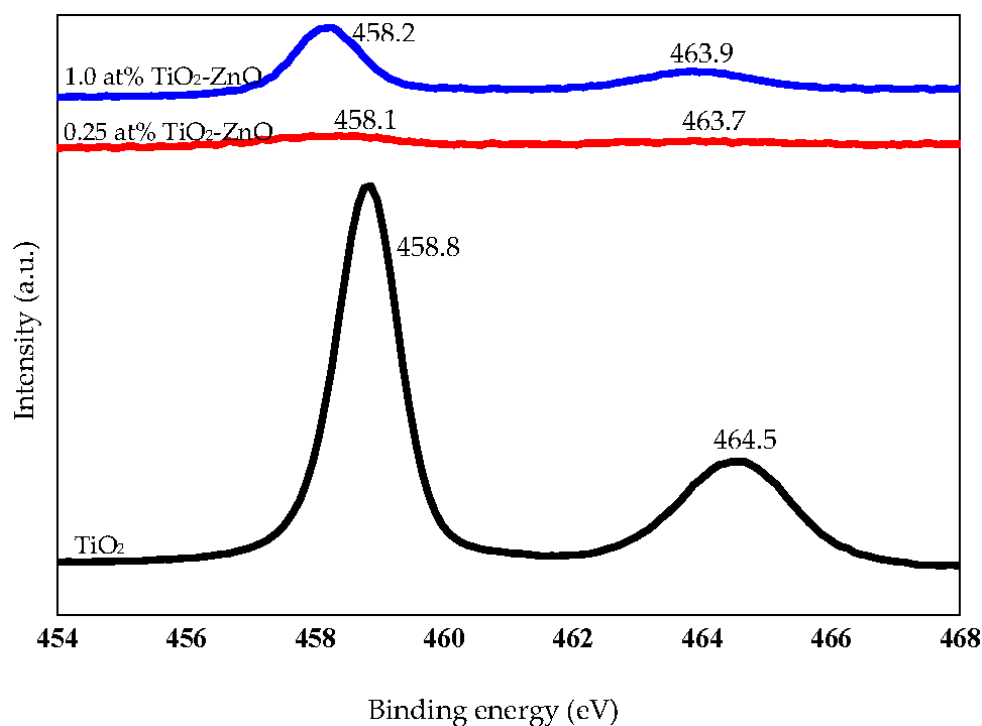
Figure 8. XPS spectra Ti2p of TiO_2, 0.25 at % TiO_2-ZnO, and 1.0 at % TiO_2-ZnO.

Table 4. Summary of XPS spectra of $Zn2p_{3/2}$, $Ti2p_{1/2}$, $Ti2p_{3/2}$, and O1s for samples TiO_2, 0.25 at % TiO_2-ZnO, 1.0 at % TiO_2-ZnO, and ZnO.

Sample	$Zn2p_{3/2}$	$Ti2p_{1/2}$	$Ti2p_{3/2}$	O1s
TiO_2	-	464.5	458.8	530.0
0.25 at % TiO_2-ZnO	1021.7	463.7	458.1	531.3
1.0 at % TiO_2-ZnO	1021.5	463.9	458.2	529.7, 531.7
ZnO	1021.8	-	-	530.5

2.3. Photoluminescence Studies

Figure 9 shows the photoluminescence study for TiO_2 loaded on ZnO nanorod film and it mainly related to some defects; for instance, zinc vacancies, zinc interstitials, oxygen vacancies, oxygen interstitials, and oxygen anti-sites. The ZnO PL spectra showed the UV emission band centered at 380 nm kept increasing with the increasing of TiO_2-ZnO cycles. Theoretically, the refractive index of TiO_2 (~2.55–2.9) is higher than wurtzite ZnO (~1.99). Therefore, TiO_2 acts as antireflection layer and with the increasing of TiO_2 cycle it may increase the absorption of light due to the oxygen anti-site at TiO_2-ZnO interface increases the adsorption of energy and it could not be transferred to ZnO [12]. The broad visible emission band (500–800 nm) is determined by the planar defect involving twin boundaries and stacking faults of Ti and O atoms at TiO_2-ZnO interface. The twin boundaries can be seen clearly from HRTEM image (Figure 1e). The stacking faults defect affects the PL peak at 500–800 nm range because Ti and O atoms were occupied in HCP ZnO interstices at TiO_2-ZnO interface. Therefore, the PL peak decreased with increasing of TiO_2 dip-coating cycle. This explanation can be supported by photocurrent density response: 0.25 at % TiO_2-Zno was higher under solar illumination as compared to bare ZnO under UV illumination. ZnO is famous for high photo reactivity under UV illumination compared to under solar illumination. However, with the collaboration of oxygen anti-site defect, TiO_2 adsorbed more energy and it could not be transferred to ZnO and produced lower photocurrent density and photoconversion efficiency.
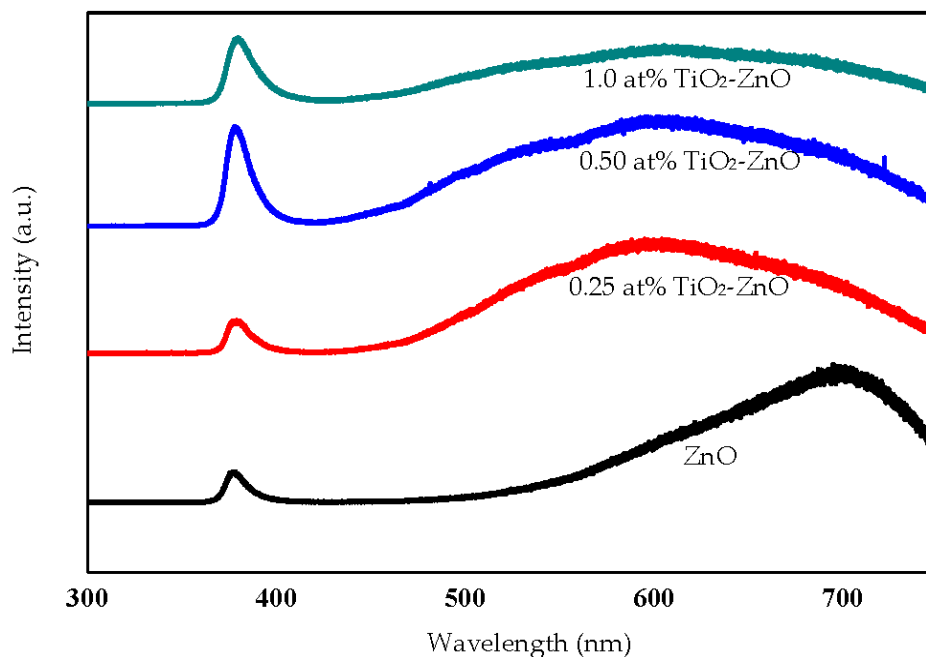
Figure 9. PL spectra of ZnO, 0.25 at % TiO_2-ZnO, 0.50 at % TiO_2-ZnO, and 1.0 at % TiO_2-ZnO (excitation: $\lambda = 514$ nm).

2.4. Photoelectrochemical Response and Photoconversion Efficiency

ZnO, with its excellent electronic properties and interfacial stability, exhibited a great PEC response for hydrogen generation. The electrical simulation for water electrolysis has been studied using the PEC response, focusing on the current density analysis (Figures 10 and 11). Meanwhile, Figure 12 shows combination of all photocurrent response under UV and solar illumination for better comparison. In this research work, TiO_2-ZnO can be found on both sides of electrode. During light illumination, the active area was only 4 cm × 1 cm which was one-sided as the TiO_2-ZnO electrode was opaque. The photoconversion efficiency (η), that is the light energy to chemical energy conversion efficiency, was subsequently calculated via Equation (1) and plotted in Figures 13 and 14 [56,57], whereby 0.25 at % TiO_2-ZnO presented the highest photocurrent density and photoconversion efficiency, regardless of whether the PEC process occurred under UV illumination or solar illumination (Figures 10b, 11b, 13b and 14b) as compared to the sample of ZnO and samples with more than one cycle of the dip-coating process. Loading ZnO with TiO_2 produced a photocurrent density of 19.78 mA/cm^2 (with V vs. Ag/AgCl), as compared to ZnO 10.94 mA/cm^2 (with V vs. Ag/AgCl) (UV illumination), 14.75 mA/cm^2 (with V vs. Ag/AgCl) and ZnO 9.06 mA/cm^2 (with V vs. Ag/AgCl) (solar illumination). Table 5 shows the summary of photocurrent density (mA/cm^2) (with V vs. Ag/AgCl) for all samples under UV illumination and solar illumination. The enhancement in photocurrent density for TiO_2 loaded on ZnO nanorod film is due to the charge-separation effect that occurred at the type-II band alignment of ZnO and TiO_2, as discussed earlier. Meanwhile, the increase in the dip-coating cycle produced a higher amount of TiO_2, and the electrons produced in TiO_2 were trapped by the oxygen adsorption and could not be transferred to ZnO [37]. From PL analysis, the oxygen anti-site defect (intrinsic defect) may also give effect to the performance of TiO_2-ZnO electrode. In Figure 12, combination of all samples showed 0.25 at % TiO_2-ZnO exhibited highest photocurrent response regardless of whether it was under UV illumination or solar illumination. This was followed by bare ZnO, which produced good photocurrent response under both illuminations. These results support the conclusion that a small amount (0.25 at % Ti) of TiO_2 is sufficient to produce excellent photocurrent response for PEC system. A photoconversion efficiency of ~2.9% (UV illumination) and ~4.3% (solar illumination), compared to ZnO, resulted from the presence of the Ti element in TiO_2 loaded on ZnO

nanorod film (below 1 at % Ti). Equally important, long nanorods in the presence of TiO_2 could harvest the excited hv better than the ZnO and other TiO_2 loaded samples. A high aspect ratio nanorods could absorb more hv, resulting in an increase in j_p and η [58].

$$\begin{aligned} \eta\,(\%) \quad &= \frac{\text{Total power output}-\text{electrical power output}}{\text{Light power input}} \times 100\% \\ &= j_p \frac{E^0_{rev}-|E_{app}|}{I_0} \times 100\% \end{aligned} \tag{1}$$

where j_p is the photocurrent density in mA·cm^{-2}; E^0_{rev} is the reversible potential (1.43 V Ag/AgCl); and $E_{app} = E_{meas} - E_{counter}$, where E_{meas} is the electrical potential (V vs. Ag/AgCl) of the working electrode under illumination, and $E_{counter}$ Is the electrical electrode (V vs. Ag/AgCl) of the working electrode at open circuit conditions.
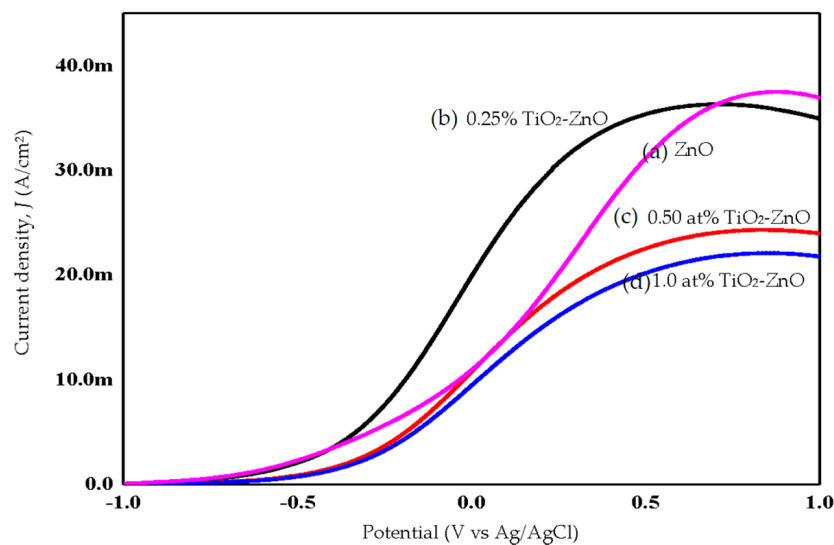

Figure 10. Photocurrent response of (**a**) ZnO; (**b**) 0.25% TiO_2-ZnO; (**c**) 0.50 at % TiO_2-ZnO; and (**d**) 1.0 at % TiO_2-ZnO under UV illumination.
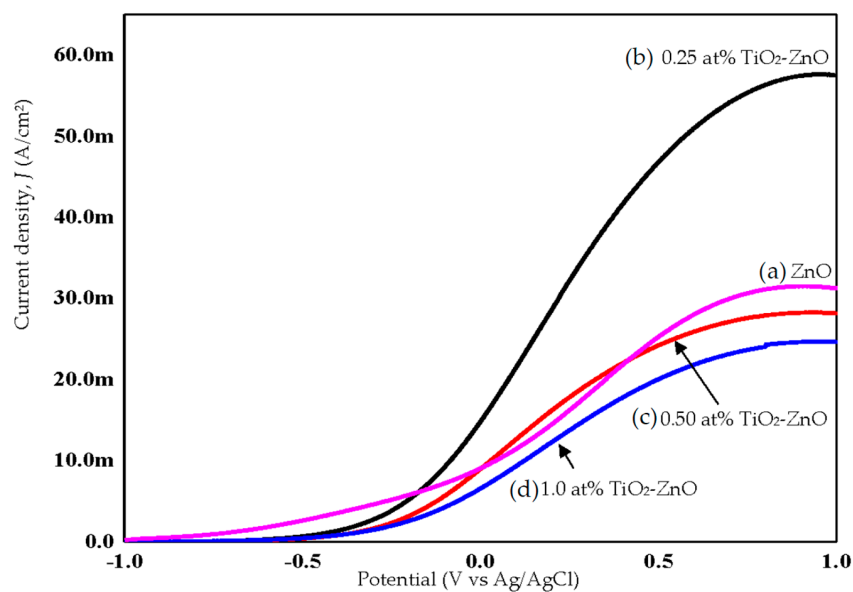
Figure 11. Photocurrent response of (**a**) ZnO; (**b**) 0.25 at % TiO_2-ZnO; (**c**) 0.50 at % TiO_2-ZnO; and (**d**) 1.0 at % TiO_2-ZnO under solar illumination.
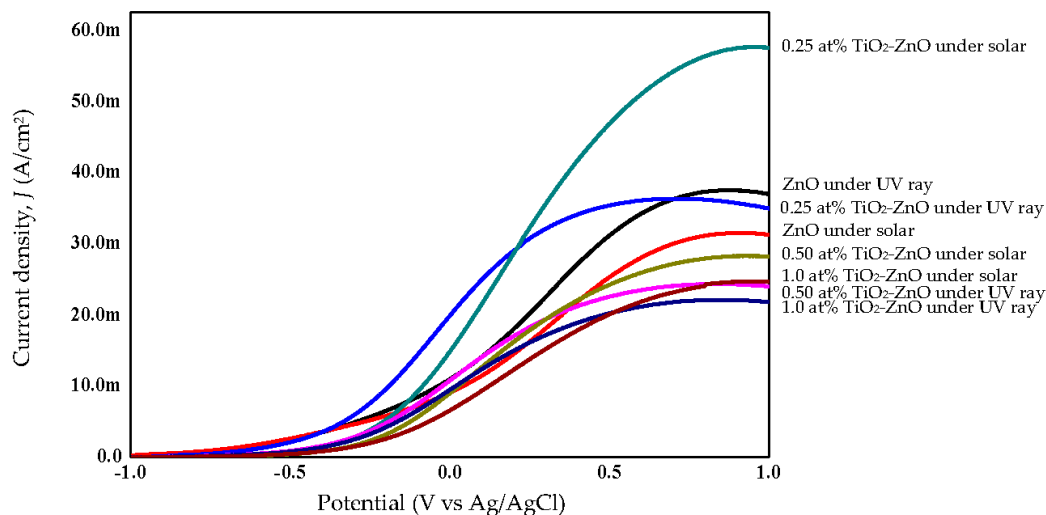
Figure 12. Photocurrent response for combination of all samples with respect to UV ray (300 nm) and solar illumination.
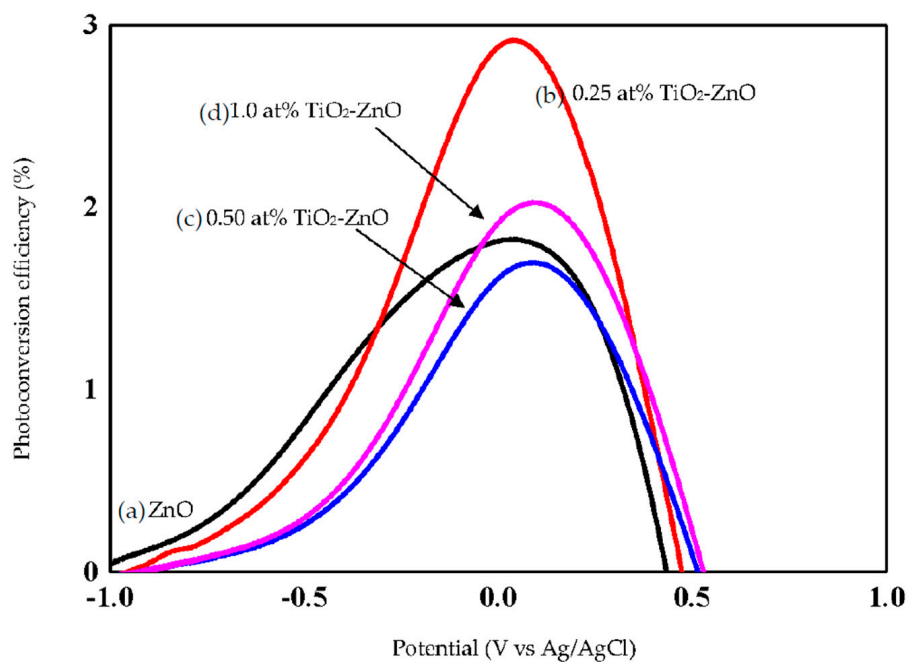

Figure 13. Photoconversion efficiency of (**a**) ZnO; (**b**) 0.25 at % TiO_2-ZnO; (**c**) 0.50 at % TiO_2-ZnO; and (**d**) 1.0 at % TiO_2-ZnO under UV illumination.

Table 5. The photocurrent density (mA/cm^2) (with V vs. Ag/AgCl) of ZnO, 0.25 at % TiO_2-ZnO, 0.50 at % TiO_2-ZnO, and 1.0 at % TiO_2-ZnO under UV illumination and solar illumination.

Sample	UV Illumination	Solar Illumination
ZnO	10.96	9.06
0.25 at % TiO_2-ZnO	19.78	14.75
0.50 at % TiO_2-ZnO	10.73	8.92
1.0 at % TiO_2-ZnO	9.40	6.52
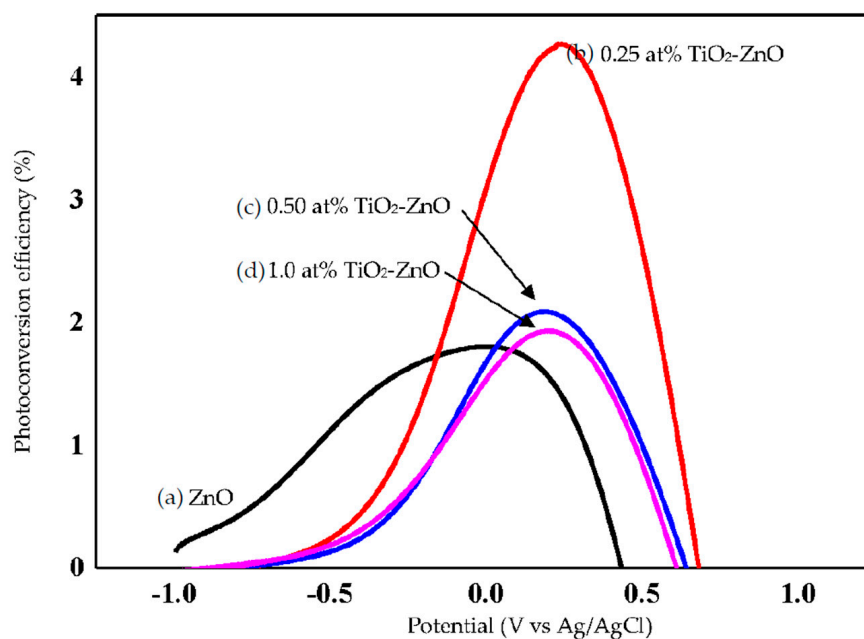
Figure 14. Photoconversion efficiency of (**a**) ZnO; (**b**) 0.25 at % TiO$_2$-ZnO; (**c**) 0.50 at % TiO$_2$-ZnO; and (**d**) 1.0 at % TiO$_2$-ZnO under solar illumination.

2.5. Optical Properties

The reflectance spectra and Tauc plot of TiO$_2$ loaded on ZnO nanorod film photocatalyst based on the dip-coating cycle are plotted in Figures 15 and 16. From the reflectance spectra, it showed that an increase in dip-coating cycle produced high reflection of incident light (Figure 15), and, therefore, produced low incident light absorption with increasing in dip-coating cycle. The band gap energies for ZnO, 0.25 at % TiO$_2$-ZnO, 0.5 at % TiO$_2$-ZnO, and 1.0 at % TiO$_2$-ZnO are 3.20 eV, 2.85 eV, 2.96 eV, and 2.98 eV, respectively (Figure 16). The band gap increased with an increase in the dip-coating cycle. However, there was no large difference between the 0.5 at % and 1.0 at % TiO$_2$ as shown by the photocurrent response readings. Theoretically, three types of semiconductor heterojunctions are organized by band alignment: straddling gap (type I), staggered gap (type II), and broken gap (type III). TiO$_2$ loaded on ZnO nanorod film had a staggered gap (type II), as proposed by previous researchers [33,59]. TiO$_2$-ZnO film exhibited band gap reduction due to the existence of planar defects [60]. Twin boundaries and stacking faults (planar defects) are correlated in band gap reduction. Based on Figure 1e, HRTEM image for TiO$_2$-ZnO film, twin boundaries can clearly be seen, which will affect the heterojunction band alignment at TiO$_2$ and ZnO interfaces. In addition, stacking faults defect affects band gap reduction by Ti and O atoms occupying interstices in the HCP wurtzite ZnO crystal structure. Therefore, E$_g$ appears at the close contact of TiO$_2$ and ZnO, and alters the electronic structure by producing resonant state (delocalized of electrons). The proposed mechanism is as follows (Figure 17), and the same mechanism has also been proposed by Hernández et al. and Fan et al. [61,62]. Electrons and holes in semiconductors are at their lowest energy states originally. Therefore, the energy gradient at the interfaces tends to spatially separate those electrons and holes that are excited by the UV illumination/solar illumination on different sides of the heterojunction. The quantum confinement effect appears at the interfaces by electrons feeling the presence of particle boundaries and responding to changes in particle size by adjusting their energy. Under illumination, the electrons are transferred from the conduction band (CB) of TiO$_2$ to CB of ZnO due to the present of potential barrier for electrons (Figure 17). During the same event, the holes are transferred from the valence band (VB) of ZnO to VB of TiO$_2$ with the presence of potential barriers for holes (Figure 17). The process isolates active electrons and holes and, hence, accelerates the decrease in the electron–hole pair recombination and erodes the increase in lifespan. These phenomena directly result in an intense

emission quenching as revealed by the photoluminescence results (Figure 9). In addition, the high aspect ratio one-dimensional structure of the ZnO nanorods also helps to decrease the recombination probability of photogenerated carriers due to an increase in the delocalization of electrons [33,59,63].
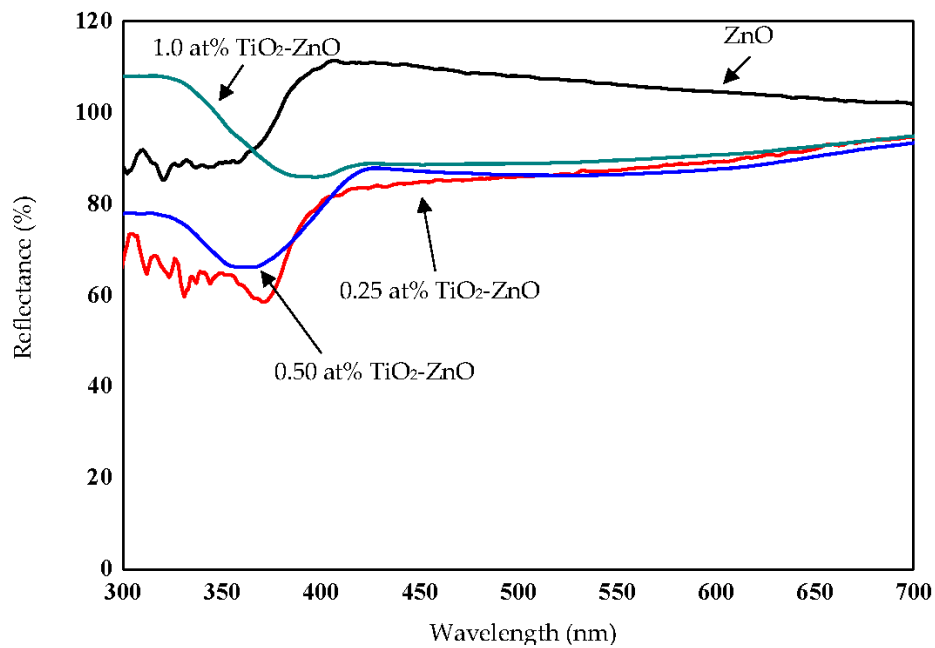

Figure 15. Reflectance spectra of ZnO, 0.25 at % TiO_2-ZnO, 0.50 at % TiO_2-ZnO, and 1.0 at % TiO_2-ZnO.
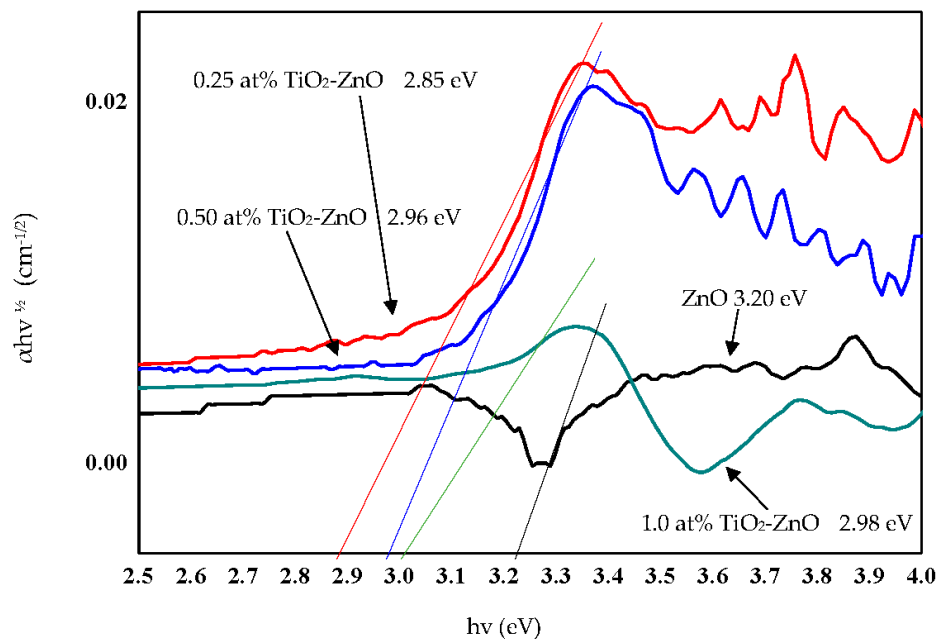

Figure 16. Tauc plot of ZnO, 0.25 at % TiO_2-ZnO, 0.50 at % TiO_2-ZnO, and 1.0 at % TiO_2-ZnO.
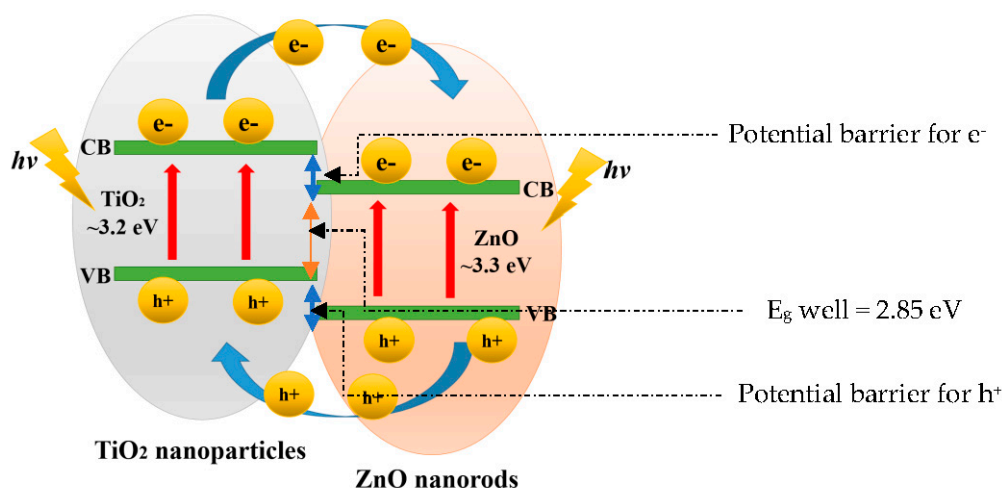
Figure 17. Illustration of staggered bandgap (type II) TiO$_2$ loaded on ZnO nanorod semiconductor and its photo-induced charge transfer and separation.

3. Materials and Methods

Most researchers implemented the hydrothermal and aqueous chemical routes for ZnO formation (Table 1). However, in this research work, electrodeposition technique has been implemented for formation of ZnO. Electrodeposition technique promised better electronic performance and stronger ZnO structure [64]. This was followed by dip-coating method, which is very economical and simple.

3.1. The Fabrication of ZnO Nanorods

Chemicals used for the electrodeposition method for ZnO nanorods formation were 0.05 mM Zinc Chloride (ZnCl$_2$), 0.1 M Potassium Chloride (KCl) and material zinc (Zn) foil (thickness 0.25 mm, 99.9% trace metals basis, Sigma-Aldrich, Saint Louis, MO, USA) under temperature 70 °C, as-prepared pH (5–6), duration 1 h, and 1 V applied potential. The electrodeposition process has been set up as a closed system of two electrodes, in which Zn foil served as cathode and platinum electrode served as anode and both electrodes were directly connected to DC power supply. The ZnO nanorods thin film has been rinsed with EMSURE ACS, 1SO, Reg. Ph Eur acetone for analysis and dried under atmosphere condition. The difference of electrodeposition method in this research work as compared to previous researches is the Zn substrate used, whereas previous researches used GaN substrate [23], Si substrate [24,65–67], steel substrate [25,68], FTO-coated glass [26], ITO-coated glass [6,69], and F-doped SnO$_2$ coated glass [70–74]. In addition, electrodeposition method in this research work is template-free as compared to previous researches that used alumina membrane templates or anodic alumina template (AAM) [75,76]. Another difference of this research work electrodeposition method was seed layer-free because previous researches reported seeded substrate such as nanosheet-like Zn seed layers and ZnO seed layer [77,78]. Acid-free is an additional difference of electrodeposition method in this research work compared to previous researches. Some researchers used organic acid, for example, benzenetetracarboxylic acid, benzoic acid, and p-toluenesulfonic acid [24]. Meanwhile, citric acid is quite popular in previous electrodeposition method [27,79].

3.2. The Formation of TiO$_2$ Nanoparticles

Chemicals used for the precipitation-peptization method were titanium (IV) isopropoxide (Sigma Aldrich, St. Louis, MO, USA, 97.0%), isopropoanol (Merck, Kirkland, QC, Canada, 99.8%), ethanol (J.Kolin, Seoul, Korea 95%) and nitric acid (merck, 65%). Solutions of nitric acid, isopropanol and deionized water were maintained in molar ratio 1:34:550 titrated with 250 mL of mixture titanium (IV) isopropoxide and isopropanol with molar ratio 1:30 under vigorous stirring for 2 h to form a

white precipitate and continue stirred for another 1 h for complete hydrolyzation. The precipitate was centrifuged and washed with ethanol and white TiO_2 gel was obtained. Subsequently, the gel was baptized in water bath with the pH 1–3 at 80 °C for 8 h until a transparent solution was obtained.

3.3. The Formation of TiO₂-ZnO Composite Thin Film

The formation of TiO_2-ZnO nanostructures composite film has been done via dip-coating method. The first step was the immersion of ZnO nanorods into TiO_2 solution (jitter-free). Second, the ZnO nanorods remained in the TiO_2 solution for less than five seconds and the deposition of very thin layer TiO_2 nanoparticles occurred while it was pulled out from TiO_2 solution. The drainage and evaporation of excess TiO_2 solution was done by drying the dipped thin film in oven at 60 °C and calcined at 400 °C for 3 h.

3.4. Characterization Methods

Field Emission Scanning Electron Microscopy (FESEM) JEOL JSM-7600F (Freising, Germany) has been used to study the morphology (including the surface and cross-sectional) of TiO_2-ZnO composite thin film. Meanwhile, elemental studies have been carried out using Hitachi Energy Dispersive X-ray Spectroscopy (EDX). The crystallinity, phase transition and photoluminescence spectra studies of TiO_2-ZnO composite thin film were carried out via Renishaw In Via Raman microscope and supported by Bruker D8 Advance equipped with EVA-Diffract Software (Karlsruhe, Germany) X-ray Dispersive (XRD) with Cu K radiation and wavelength $\lambda = 1.5418$ Å. The photocurrent densities were obtained from photoelectrochemical cell consisted of three-electrodes (TiO_2-ZnO nanostructures composite film (anode), platinum electrode (cathode), and Ag/AgCl in saturated KCl electrode (reference electrode)). All electrodes were immersed in 1 vol% ethylene glycol added to 1 M sodium hydroxide (NaOH). Small amount of ethylene glycol has been used as sacrificial agent during PEC procedure. Ethylene glycol worked as electron donor during PEC procedure. It supplied electron with the photogenerated VB holes for increase the electron–holes separation [80]. Light source with AM1.5 filter has been used for both UV and solar illumination (Newport model 74010) focused on the PEC cell. The light intensity was 0.652 Wcm^{-2}. Meanwhile, current-applied potential was measured by using Metrohm Autolab PGSTAT204 (Herisau, Switzerland), with procedure linear sweep voltammetry potentiostatic (-1 to 1 V potential applied). The illuminated area was one-sided and, therefore, active area was 4 cm $\times$ 1 cm.

4. Conclusions

In summary, fine-tuning the content of TiO_2 loaded on ZnO nanorod film is important to develop an efficient solar driven PEC system through dip-coating technique. An improvement in the photocurrent density and photoconversion efficiency was observed in the 0.25 at % TiO_2 loaded on ZnO nanorod film with maximum value photocurrent density of 19.78 mA/cm^2 (with V vs. Ag/AgCl) (UV illumination) and 14.75 mA/cm^2 (with V vs. Ag/AgCl) (solar illumination) with photoconversion efficiency of ~2.9% (UV illumination) and ~4.3% (solar illumination). This finding is attributed to the excellent performance by promoting an impurity level in the binary system. In this case, the optimum 0.25 at % of TiO_2 content acted as an electron acceptor, which was beneficial for the effective separation of the photo-induced charge carriers. However, the excessive TiO_2 content (>0.50 at % Ti) loaded on ZnO nanorod film resulted in poor PEC performance. A suggestion for future research work is to prepare a mild TiO_2 solution, with simple coating process in order to study the effectiveness TiO_2-ZnO properties.

References

1. Navarro Yerga, R.M.; Alvarez Galván, M.C.; del Valle, F.; Villoria de la Mano, J.A.; Fierro, J.L. Water Splitting on Semiconductor Catalysts under Visible-Light Irradiation. *ChemSusChem* **2009**, *2*, 471–485. [CrossRef] [PubMed]

2. Kim, Y.K.; Park, H. Light-harvesting multi-walled carbon nanotubes and CdS hybrids: Application to photocatalytic hydrogen production from water. *Energy Environ. Sci.* **2011**, *4*, 685–694. [CrossRef]

3. Bahadur, H.; Srivastava, A.K.; Sharma, R.K.; Chandra, S. Morphologies of sol-gel derived thin films of ZnO using different precursor materials and their nanostructures. *Nanoscale Res. Lett.* **2007**, *2*, 469–475. [CrossRef]

4. Bornand, V.; Mezy, A. An alternative approach for the oriented growth of ZnO nanostructures. *Mater. Lett.* **2011**, *65*, 1363–1366. [CrossRef]

5. Aziz, N.S.; Mahmood, M.R.; Yasui, K.; Hashim, A.M. Seed/catalyst-free vertical growth of high-density electrodeposited zinc oxide nanostructures on a single-layer graphene. *Nanoscale Res. Lett.* **2014**, *9*, 1–7. [CrossRef] [PubMed]

6. Dai, S.; Li, Y.; Du, Z.; Carter, K.R. Electrochemical deposition of ZnO hierarchical nanostructures from hydrogel coated electrodes. *J. Electrochem. Soc.* **2013**, *160*, D156–D162. [CrossRef]

7. Kim, Y.J.; Hadiyawarman; Yoon, A.; Kim, M.; Yi, G.C.; Liu, C. Hydrothermally grown ZnO nanostructures on few-layer graphene sheets. *Nanotechnology* **2011**, *22*. [CrossRef] [PubMed]

8. Du, J.; Liu, Z.; Huang, Y.; Gao, Y.; Han, B.; Li, W.; Yang, G. Control of ZnO morphologies via surfactants assisted route in the subcritical water. *J. Cryst. Growth* **2005**, *280*, 126–134. [CrossRef]

9. Lepot, N.; van Bael, M.K.; van den Rul, H.; D'Haen, J.; Peeters, R.; Franco, D.; Mullens, J. Synthesis of ZnO nanorods from aqueous solution. *Mater. Lett.* **2007**, *61*, 2624–2627. [CrossRef]

10. Park, W.I.; Kim, D.H.; Jung, S.-W.; Yi, G. Metalorganic vapor-phase epitaxial growth of vertically well-aligned ZnO nanorods. *Appl. Phys. Lett.* **2002**, *80*, 4232–4234. [CrossRef]

11. Oliveira, M.M.; Schnitzler, D.C.; Zarbin, A.J. (Ti, Sn) O$_2$ Mixed Oxides Nanoparticles Obtained by the Sol-Gel Route. *Chem. Mater.* **2003**, *15*, 1903–1909. [CrossRef]

12. Andersson, M.; Österlund, L.; Ljungström, S.; Palmqvist, A. Preparation of nanosize anatase and rutile TiO$_2$ by hydrothermal treatment of microemulsions and their activity for photocatalytic wet oxidation of phenol. *J. Phys. Chem. B* **2002**, *106*, 10674–10679. [CrossRef]

13. Varghese, N.; Panchakarla, L.S.; Hanapi, M.; Govindaraj, A.; Rao, C.N.R. Solvothermal synthesis of nanorods of ZnO, N-doped ZnO and CdO. *Mater. Res. Bull.* **2007**, *42*, 2117–2124. [CrossRef]

14. Yiamsawas, D.; Boonpavanitchakul, K.; Kangwansupamonkon, W. Preparation of ZnO nanostructures by solvothermal method. *J. Microsc. Soc. Thail.* **2009**, *23*, 75–78.

15. Lee, H.K.; Yu, J.S. Growth Parameter Dependent Structural and Optical Properties of ZnO Nanostructures on Si Substrate by a Two-Zone Thermal CVD. *J. Nanosci. Nanotechnol.* **2012**, *12*, 3123–3129. [CrossRef] [PubMed]

16. Khranovskyy, V.; Yakimova, R. Morphology engineering of ZnO nanostructures. *Phys. B Condens. Matter* **2012**, *407*, 1533–1537. [CrossRef]

17. Kim, K.-S.; Kim, H.W. Synthesis of ZnO nanorod on bare Si substrate using metal organic chemical vapor deposition. *Phys. B Condens. Matter* **2003**, *328*, 368–371. [CrossRef]

18. Saitoh, H.; Satoh, M.; Tanaka, N.; Ueda, Y.; Ohshio, S. Homogeneous growth of zinc oxide whiskers. *Jpn. J. Appl. Phys.* **1999**, *38*, 6873. [CrossRef]

19. Clavel, G.; Marichy, C.; Willinger, M.; Ravaine, S.; Zitoun, D.; Pinna, N. CoFe$_2$O$_4$-TiO$_2$ and CoFe$_2$O$_4$-ZnO Thin Film Nanostructures Elaborated from Colloidal Chemistry and Atomic Layer Deposition. *Langmuir* **2010**, *26*, 18400–18407. [CrossRef] [PubMed]

20. Leskelä, M.; Ritala, M. Atomic layer deposition (ALD): From precursors to thin film structures. *Thin Solid Films* **2002**, *409*, 138–146. [CrossRef]

21. Solís-Pomar, F.; Martínez, E.; Meléndrez, M.F.; Pérez-Tijerina, E. Growth of vertically aligned ZnO nanorods using textured ZnO films. *Nanoscale Res. Lett.* **2011**, *6*, 1–11. [CrossRef] [PubMed]

22. Wu, M.-K.; Chen, M.; Tsai, F.; Yang, J.; Shiojiri, M. Fabrication of ZnO nanopillars by atomic layer deposition. *Mater. Trans.* **2010**, *51*, 253–255. [CrossRef]

23. Rousset, J.; Lincot, D. Low Temperature Electrodeposition of Zinc Oxide Layers as Transparent Conducting Oxide Window Layers for Cigs Solar Cells. In Proceedings of the 2009 34th IEEE Photovoltaic Specialists Conference, Philadelphia, PA, USA, 7–12 June 2009; Volumes 1–3, pp. 698–703.

24. Liu, W.L.; Chang, Y.C.; Hsieh, S.H.; Chen, W.J. Effects of Anions in electrodeposition baths on morphologies of Zinc Oxide Thin Films. *Int. J. Electrochem. Sci.* **2013**, *8*, 983–990.

25. Šulčiūtė, A.; Valatka, E. Electrodeposition and photoelectrocatalytic activity of ZnO films on AISI 304 type steel. *Mater. Sci.* **2012**, *18*, 318–324. [CrossRef]

26. Khrypunov, G.; Klochko, N.; Volkova, N.; Kopach, V.; Lyubov, V.; Klepikova, K. Pulse and direct current electrodeposition of zinc oxide layers for solar cells with extra thin absorbers. In Proceedings of the World Renewable Energy Congress (WREC-2011), Linköping, Sweden, 8–13 May 2011.

27. Li, G.-R.; Lu, X.H.; Qu, D.L.; Yao, C.Z.; Zheng, F.L.; Bu, Q.; Dawa, C.R.; Tong, Y.X. Electrochemical growth and control of ZnO dendritic structures. *J. Phys. Chem. C* **2007**, *111*, 6678–6683. [CrossRef]

28. Abd-Ellah, M.; Moghimi, N.; Zhang, L.; Heinig, N.F.; Zhao, L.; Thomas, J.P.; Leung, K. Effect of Electrolyte Conductivity on Controlled Electrochemical Synthesis of Zinc Oxide Nanotubes and Nanorods. *J. Phys. Chem. C* **2013**, *117*, 6794–6799. [CrossRef]

29. Anpo, M.; Nakaya, H.; Kodama, S.; Kubokawa, Y.; Domen, K.; Onishi, T. Photocatalysis over binary metal oxides. Enhancement of the photocatalytic activity of titanium dioxide in titanium-silicon oxides. *J. Phys. Chem.* **1986**, *90*, 1633–1636. [CrossRef]

30. Zhang, H.; Chen, G.; Bahnemann, D.W. Photoelectrocatalytic materials for environmental applications. *J. Mater. Chem.* **2009**, *19*, 5089–5121. [CrossRef]

31. Lai, C.W.; Juan, J.C.; Ko, W.B.; Hamid, S.B.A. An overview: Recent development of titanium oxide nanotubes as photocatalyst for dye degradation. *Int. J. Photoenergy* **2014**, *2014*. [CrossRef]

32. Bessegato, G.G.; Guaraldo, T.T.; Zanoni, M.V.B. Enhancement of Photoelectrocatalysis Efficiency by Using Nanostructured Electrodes. *Mod. Electrochem. Methods Nano Surf. Corros. Sci.* **2014**, 271–391. [CrossRef]

33. Shao, D.; Sun, H.; Xin, G.; Lian, J.; Sawyer, S. High quality ZnO–TiO$_2$ core–shell nanowires for efficient ultraviolet sensing. *Appl. Surf. Sci.* **2014**, *314*, 872–876. [CrossRef]

34. Hernández, S.; Cauda, V.; Hidalgo, D.; Rivera, V.F.; Manfredi, D.; Chiodoni, A.; Pirri, F.C. Fast and low-cost synthesis of 1D ZnO–TiO$_2$ core–shell nanoarrays: Characterization and enhanced photo-electrochemical performance for water splitting. *J. Alloys Compd.* **2014**, *615*, S530–S537. [CrossRef]

35. Dao, T.; Dang, C.; Han, G.; Hoang, C.; Yi, W.; Narayanamurti, V.; Nagao, T. Chemically synthesized nanowire TiO$_2$/ZnO core-shell pn junction array for high sensitivity ultraviolet photodetector. *Appl. Phys. Lett.* **2013**, *103*, 193119. [CrossRef]

36. Lin, L.; Yang, Y.; Men, L.; Wang, X.; He, D.; Chai, Y.; Zhao, B.; Ghoshroy, S.; Tang, Q. A highly efficient TiO$_2$@ZnO n–p–n heterojunction nanorod photocatalyst. *Nanoscale* **2013**, *5*, 588–593. [CrossRef] [PubMed]

37. Panigrahi, S.; Basak, D. Core–shell TiO$_2$@ ZnO nanorods for efficient ultraviolet photodetection. *Nanoscale* **2011**, *3*, 2336–2341. [CrossRef] [PubMed]

38. Exarhos, G.J.; Sharma, S.K. Influence of processing variables on the structure and properties of ZnO films. *Thin Solid Films* **1995**, *270*, 27–32. [CrossRef]

39. Schumm, M.; Koerdel, M.; Morhange, J.; Golacki, Z.; Grasza, K.; Skupinski, P.; Szuszkiewicz, W.; Zhou, H.; Malik, V.; Kalt, H. Analysis of the vibrational properties of Zn1-xCoxO by Raman spectroscopy. *J. Phys. Conf. Ser.* **2007**, *92*. [CrossRef]

40. Alim, K.A.; Fonoberov, V.A.; Balandin, A.A. Origin of the optical phonon frequency shifts in ZnO quantum dots. *Appl. Phys. Lett.* **2005**, *86*, 53103. [CrossRef]

41. Zhang, R.; Yin, P.G.; Wang, N.; Guo, L. Photoluminescence and Raman scattering of ZnO nanorods. *Solid State Sci.* **2009**, *11*, 865–869. [CrossRef]

42. Naumkin, A.V.; Kraut-Vass, A.; Gaarenstroom, S.W.; Powell, C.J. *NIST X-ray Photoelectron Spectroscopy Database*; National Institute of Standards and Technology (NIST): Gaithersburg, MD, USA, 2012.

43. Nefedov, V.; Salyn, Y.V.; Leonhardt, G.; Scheibe, R. A comparison of different spectrometers and charge corrections used in X-ray photoelectron spectroscopy. *J. Electron Spectrosc. Relat. Phenom.* **1977**, *10*, 121–124. [CrossRef]

44. Hosseini, S.; Sarsari, I.A.; Kameli, P.; Salamati, H. Effect of Ag doping on structural, optical, and photocatalytic properties of ZnO nanoparticles. *J. Alloys Compd.* **2015**, *640*, 408–415. [CrossRef]

45. Sahu, R.K.; Ganguly, K.; Mishra, T.; Mishra, M.; Ningthoujam, R.; Roy, S.; Pathak, L. Stabilization of intrinsic defects at high temperatures in ZnO nanoparticles by Ag modification. *J. Colloid Interface Sci.* **2012**, *366*, 8–15. [CrossRef] [PubMed]

46. Zhang, X.; Ganguly, K.; Mishra, T.; Mishra, M.; Ningthoujam, R.; Roy, S.; Pathak, L. Effect of aspect ratio and surface defects on the photocatalytic activity of ZnO nanorods. *Sci. Rep.* **2014**, *4*. [CrossRef] [PubMed]

47. Al-Gaashani, R.; Radiman, S.; Daud, A.R.; Tabet, N.; Al-Douri, Y. XPS and optical studies of different morphologies of ZnO nanostructures prepared by microwave methods. *Ceram. Int.* **2013**, *39*, 2283–2292. [CrossRef]

48. Zheng, J.; Song, J.; Li, X.; Jiang, Q.; Lian, J. Experimental and first-principle investigation of Cu-doped ZnO ferromagnetic powders. *Cryst. Res. Technol.* **2011**, *46*, 1143–1148. [CrossRef]

49. Chong, M.N.; Jin, B.; Chow, C.W.; Saint, C. Recent developments in photocatalytic water treatment technology: A review. *Water Res.* **2010**, *44*, 2997–3027. [CrossRef] [PubMed]

50. Chen, Y.-W.; Lee, D.-S.; Chen, H.-J. Preferential oxidation of CO in H$_2$ stream on Au/ZnO–TiO$_2$ catalysts. *Int. J. Hydrogen Energy* **2012**, *37*, 15140–15155. [CrossRef]

51. Soares, J.M.; Morrall, P.; Crossley, A.; Harris, P.; Bowker, M. Catalytic and noncatalytic CO oxidation on Au/TiO$_2$ catalysts. *J. Catal.* **2003**, *219*, 17–24. [CrossRef]

52. Casaletto, M.; Longo, A.; Martorana, A.; Prestianni, A.; Venezia, A. XPS study of supported gold catalysts: The role of Au0 and Au+ δ species as active sites. *Surf. Interface Anal.* **2006**, *38*, 215–218. [CrossRef]

53. Moreau, F.; Bond, G.C. Influence of the surface area of the support on the activity of gold catalysts for CO oxidation. *Catal. Today* **2007**, *122*, 215–221. [CrossRef]

54. Tabakova, T.; Idakiev, V.; Andreeva, D.; Mitov, I. Influence of the microscopic properties of the support on the catalytic activity of Au/ZnO, Au/ZrO$_2$, Au/Fe$_2$O$_3$, Au/Fe$_2$O$_3$–ZnO, Au/Fe$_2$O$_3$–ZrO$_2$ catalysts for the WGS reaction. *Appl. Catal. A Gen.* **2000**, *202*, 91–97. [CrossRef]

55. Moulder, J.F.; Chastain, J.; King, R.C. *Handbook of X-ray Photoelectron Spectroscopy: A Reference Book of Standard Spectra for Identification and Interpretation of XPS Data*; Physical Electronics Eden Prairie: Chanhassen, MN, USA, 1995.

56. Shankar, K.; Mor, G.K.; Prakasam, H.E.; Yoriya, S.; Paulose, M.; Varghese, O.K.; Grimes, C.A. Highly-ordered TiO$_2$ nanotube arrays up to 220 μm in length: Use in water photoelectrolysis and dye-sensitized solar cells. *Nanotechnology* **2007**, *18*, 065707. [CrossRef]

57. Sun, Y.; Wang, G.; Yan, K. TiO$_2$ nanotubes for hydrogen generation by photocatalytic water splitting in a two-compartment photoelectrochemical cell. *Int. J. Hydrogen Energy* **2011**, *36*, 15502–15508. [CrossRef]

58. Ong, K.G.; Varghese, O.K.; Mor, G.K.; Grimes, C.A. Numerical simulation of light propagation through highly-ordered titania nanotube arrays: Dimension optimization for improved photoabsorption. *J. Nanosci. Nanotechnol.* **2005**, *5*, 1801–1808. [CrossRef] [PubMed]

59. Cheng, C.; Amini, A.; Zhu, C.; Xu, Z.; Song, H.; Wang, N. Enhanced photocatalytic performance of TiO$_2$-ZnO hybrid nanostructures. *Sci. Rep.* **2014**, *4*. [CrossRef] [PubMed]

60. Asthana, A.; Momeni, K.; Prasad, A.; Yap, Y.; Yassar, R. On the correlation of crystal defects and band gap properties of ZnO nanobelts. *Appl. Phys. A* **2011**, *105*, 909–914. [CrossRef]

61. Hernández, S.; Cauda, V.; Chiodoni, A.; Dallorto, S.; Sacco, A.; Hidalgo, D.; Celasco, E.; Pirri, C.F. Optimization of 1D ZnO@ TiO$_2$ Core–Shell Nanostructures for Enhanced Photoelectrochemical Water Splitting under Solar Light Illumination. *ACS Appl. Mater. Interfaces* **2014**, *6*, 12153–12167. [CrossRef] [PubMed]

62. Fan, J.; Zamani, R.; Fàbrega, C.; Shavel, A.; Flox, C.; Ibáñez, M.; Andreu, T.; López, A.M.; Arbiol, J.; Morante, J.R. Solution-growth and optoelectronic performance of ZnO: Cl/TiO$_2$ and ZnO: Cl/ZnxTiOy/TiO$_2$ core–shell nanowires with tunable shell thickness. *J. Phys. D Appl. Phys.* **2012**, *45*, 415301. [CrossRef]

63. Leelavathi, A.; Madras, G.; Ravishankar, N. Origin of enhanced photocatalytic activity and photoconduction in high aspect ratio ZnO nanorods. *Phys. Chem. Chem. Phys.* **2013**, *15*, 10795–10802. [CrossRef] [PubMed]

64. Kishwar, S.; Hasan, K.U.; Alvi, N.; Klason, P.; Nur, O.; Willander, M. A comparative study of the electrodeposition and the aqueous chemical growth techniques for the utilization of ZnO nanorods on p-GaN for white light emitting diodes. *Superlattices Microstruct.* **2011**, *49*, 32–42. [CrossRef]

65. Izaki, M.; Watase, S.; Takahashi, H. Room-temperature ultraviolet light-emitting zinc oxide micropatterns prepared by low-temperature electrodeposition and photoresist. *Appl. Phys. Lett.* **2003**, *83*, 4930–4932. [CrossRef]

66. Dalchiele, E.; Giorgi, P.; Marotti, R.; Martın, F.; Ramos-Barrado, J.; Ayouci, R.; Leinen, D. Electrodeposition of ZnO thin films on n-Si (100). *Sol. Energy Mater. Sol. Cells* **2001**, *70*, 245–254. [CrossRef]

67. Postels, B.; Bakin, A.; Wehmann, H.-H.; Suleiman, M.; Weimann, T.; Hinze, P.; Waag, A. Electrodeposition of ZnO nanorods for device application. *Appl. Phys. A* **2008**, *91*, 595–599. [CrossRef]

68. Li, M.C.; Jiang, L.L.; Zhang, W.Q.; Qian, Y.H.; Luo, S.Z.; Shen, J.N. Electrodeposition of nanocrystalline zinc from acidic sulfate solutions containing thiourea and benzalacetone as additives. *J. Solid State Electrochem.* **2007**, *11*, 549–553. [CrossRef]

69. Sun, S.J.; Jiao, S.J.; Zhang, K.J.; Wang, D.B.; Gao, S.Y.; Li, H.T.; Wang, J.Z.; Yu, Q.J.; Guo, F.Y.; Zhao, L.C. Nucleation effect and growth mechanism of ZnO nanostructures by electrodeposition from aqueous zinc nitrate baths. *J. Cryst. Growth* **2012**, *359*, 15–19. [CrossRef]

70. Zhang, L.S.; Chen, Z.G.; Tang, Y.W.; Jia, Z.J. Low temperature cathodic electrodeposition of nanocrystalline zinc oxide thin films. *Thin Solid Films* **2005**, *492*, 24–29. [CrossRef]

71. Lupan, O.; Pauporté, T.; Viana, B.; Aschehoug, P. Electrodeposition of Cu-doped ZnO nanowire arrays and heterojunction formation with p-GaN for color tunable light emitting diode applications. *Electrochim. Acta* **2011**, *56*, 10543–10549. [CrossRef]

72. Yoshida, T.; Komatsu, D.; Shimokawa, N.; Minoura, H. Mechanism of cathodic electrodeposition of zinc oxide thin films from aqueous zinc nitrate baths. *Thin Solid Films* **2004**, *451*, 166–169. [CrossRef]

73. Goux, A.; Pauporté, T.; Chivot, J.; Lincot, D. Temperature effects on ZnO electrodeposition. *Electrochim. Acta* **2005**, *50*, 2239–2248. [CrossRef]

74. Inamdar, A.I.; Mujawar, S.H.; Barman, S.R.; Bhosale, P.N.; Patil, P.S. The effect of bath temperature on the electrodeposition of zinc oxide thin films via an acetate medium. *Semicond. Sci. Technol.* **2008**, *23*, 6. [CrossRef]

75. Fan, Z.; Lu, J.G. Zinc oxide nanostructures: Synthesis and properties. *J. Nanosci. Nanotechnol.* **2005**, *5*, 1561–1573. [CrossRef] [PubMed]

76. Ramírez, D.; Gómez, H.; Riveros, G.; Schrebler, R.; Henríquez, R.; Lincot, D. Effect of Zn (II) concentration on the morphology of zinc oxide nanorods during electrodeposition on very thin alumina membrane templates. *J. Phys. Chem. C* **2010**, *114*, 14854–14859. [CrossRef]

77. Zarębska, K.; Kwiatkowski, M.; Gniadek, M.; Skompska, M. Electrodeposition of Zn (OH)$_2$, ZnO thin films and nanosheet-like Zn seed layers and influence of their morphology on the growth of ZnO nanorods. *Electrochim. Acta* **2013**, *98*, 255–262. [CrossRef]

78. Zoolfakar, A.S.; Kadir, R.A.; Rani, R.A.; Balendhran, S.; Liu, X.; Kats, E.; Bhargava, S.K.; Bhaskaran, M.; Sriram, S.; Zhuiykov, S. Engineering electrodeposited ZnO films and their memristive switching performance. *Phys. Chem. Chem. Phys.* **2013**, *15*, 10376–10384. [CrossRef] [PubMed]

79. Inamdar, A.; Mujawar, S.; Patil, P. The influences of complexing agents on growth of zinc oxide thin films from zinc acetate bath and associated kinetic parameters. *Int. J. Electrochem. Sci.* **2007**, *2*, 797–808.

80. Liao, C.-H.; Huang, C.-W.; Wu, J. Hydrogen production from semiconductor-based photocatalysis via water splitting. *Catalysts* **2012**, *2*, 490–516. [CrossRef]